MULTI-WAVELENGTH STUDY OF FLARING ACTIVITY IN BL Lac OBJECT S5 0716+714 DURING THE 2015 OUTBURST

SUNIL CHANDRA[1], HAOCHENG ZHANG[2,3], PANKAJ KUSHWAHA[1], K. P. SINGH[1], M. BÖTTCHER[4], NAVPREET KAUR[5], AND K. S. BALIYAN[5]

[1] Department of Astronomy & Astrophysics, Tata Institute of Fundamental Research, Mumbai 400005, India
[2] Astrophysical Institute, Department of Physics and Astronomy, Ohio University, Athens, OH 45701, USA
[3] Theoretical Division, Los Alamos National Laboratory, Los Alamos, NM 87545, USA
[4] Centre for Space Research, North-West University, Potchefstroom 2531, South Africa
[5] Physical Research Laboratory, Ahmedabad 380009, India

ABSTRACT

We present a detailed investigation of the flaring activity observed from a BL Lac object, S5 0716+714 , during its brightest ever optical state in the second half of 2015 January. Observed almost simultaneously in the optical, X-rays, and γ-rays, a significant change in the degree of optical polarization (PD) and a swing in the position angle (PA) of polarization were recorded. A TeV (VHE) detection was also reported by the MAGIC consortium during this flaring episode. Two prominent sub-flares, peaking about five days apart, were seen in almost all of the energy bands. The multi-wavelength light curves, spectral energy distribution, and polarization are modeled using the time-dependent code developed by Zhang et al. This model assumes a straight jet threaded by large-scale helical magnetic fields taking into account the light travel time effects, incorporating synchrotron flux and polarization in 3D geometry. The rapid variation in PD and rotation in PA are most likely due to reconnections happening in the emission region in the jet, as suggested by the change in the ratio of toroidal to poloidal components of the magnetic field during the quiescent and flaring states.

Key word: BL Lacertae objects: individual (S5 0716+714)

1. INTRODUCTION

Blazars are an extreme subclass of active galactic nuclei known to posses extremely collimated relativistic jets that are perpendicular to the plane of the accretion disk and oriented at very small angles ($<15°$) to our line of sight (LOS; Urry & Padovani 1995, 2000). Such a close alignment of the jet to the LOS leads to the relativistic boosting of the jet emission, which dominates the blazar emission. The spectral energy distribution (SED) of a blazar typically exhibits bi-modality with two broad bumps: one peaks between sub-millimeter and UV/X-ray energies, and the other peaks somewhere at MeV–GeV energies. The low-energy part of the SED is well established as being due to the synchrotron process in the relativistic jet (Urry & Mushotzky 1982), with other non-jet components, like the disk, torus, broad-line region (BLR), etc., also making significant contributions to several sources, albeit in narrow energy range (Ghisellini et al. 2009; Kushwaha et al. 2014; Nalewajko et al. 2014). The high-energy bump, on the other hand, is poorly understood and, according to one approach, is thought to arise from inverse Compton (IC) scattering of low-energy seed photons by highly energetic leptons (e^+/e^-) in the jet. If synchrotron photons originating in the same population of high-energy leptons are upscattered to high energies, then the process is known as synchrotron self Compton (SSC; Ghisellini et al. 1985; Bloom & Marscher 1996; Sokolov et al. 2004). In those cases where the seed photons are external to the jet, namely, from the disk, torus, BLR, and/or sometimes even Cosmic Wave Background Radiation, then the process is known as external Comptonization (Dermer et al. 1992; Blazejowski et al. 2000; Sikora et al. 1994, 2009; Agudo et al. 2011).

The emission from blazars shows an enormous amount of variability at almost all frequencies. Since the central engine is not resolvable by any existing facility, the variability provides a useful tool to diagnose the physical mechanisms responsible for the emission, thanks to the availability of quasi-simultaneous data at various energies from space-based (e.g., *Fermi, Swift,* etc.) and many ground-based observatories. Optical polarization observations can sufficiently constrain many of the jet properties, e.g., the strength and nature of the magnetic field, the geometry of the jet, the physical processes, etc., provided that these observations are properly supplemented by variability information at other energies. High-energy γ-ray flares are mostly followed by activity at lower energies, with the few exceptions of orphan flares. The observability of emission from a blazar jet at a particular energy may be dependent on the opacity of the emission region at that wavelength. Therefore, in this scenario, the location of the dissipation region becomes an important factor for the nature of the variability seen across the electromagnetic spectrum. In other words, a multi-wavelength variability study of blazars can also provide us with information about the location of the emission region in the jet (Marscher et al. 2010; Orienti et al. 2013).

In the literature, some cases of rotation or swing in the position angle (PA) have been reported during high-energy flares in blazars (Abdo et al. 2010; Marscher 2014; Zhang et al. 2014). Since it is dependent only on the orientation of the shock and the magnetic field threading it, PA provides a unique tool to understand the acceleration mechanisms and behavior of the shocked plasma. Several models have been proposed to understand the PA swings, however, only two of them are currently capable of reproducing multi-wavelength light curves, time-dependent SEDs, and multi-frequency polarization simultaneously. The first model, known as the Turbulent, Extreme Multi-zone Model (TEMZ), suggested by Marscher (2014), assumes that the emission region is comprised of a turbulent chaotic magnetic field with a large number of small

regions of ordered small-scale magnetic fields called "cells." A proper accounting of the time-dependent contributions from individual cells to the total emission is performed to simulate the observables. The second approach, known as the Helical Magnetic Field Model (HMFM), proposed by Zhang et al. (2014), assumes a large-scale ordered helical magnetic field with a more rigorous and proper accounting for light travel time effects (LTTEs) for individual zones to recreate the SEDs, light curves, and polarization.

The blazar S5 0716+714, at a redshift, z, of 0.31 (Nilsson et al. 2008), is one of the brightest BL Lac objects that is highly variable from radio to γ-ray energies with a very high duty cycle (Wagner et al. 1996). In the SED-based classification scheme, S5 0716+714 is sub-classified as an intermediate-energy peaked BL Lac object (IBL; Giommi et al. 1999) and is also confirmed based on the concave shape of its X-ray (0.1–10.0 keV) spectrum (Ferrero et al. 2006; Foschini et al. 2006). The concave shape of the X-ray spectrum is indicative of the presence of a tail from the synchrotron emission (falling tail) and a flatter part from the IC spectrum (rising tail). This object has been detected in the MeV energy range several times at different flux levels by the EGRET detector on board the *Compton Gamma-ray Observatory* (CGRO; Hartman et al. 1999; Nandikotkur et al. 2007). In 2008, *AstroRivelatore Gamma a Immagini Leggero* (*AGILE*) reported the detection of variable γ-ray flux with a peak flux density above the maximum reported by EGRET (Chen et al. 2008). S5 0716 +714 is also in the *Fermi*-Large Area Telescope (LAT) bright source list (Abdo et al. 2009). MAGIC first detected this source in VHE γ-rays during 2007 November ($F_{>0.4\,\text{TeV}} \sim 0.8 \times 10^{-11}$ erg cm^{-2} s^{-1}) and later with a much larger flux ($F_{>0.4\,\text{TeV}} \sim 7.5 \times 10^{-11}$ erg cm^{-2} s^{-1}) at 5.8σ in 2008, April. A similar trend was also seen in the optical (Anderhub et al. 2009) while the source was in a historically high state in X-rays (Giommi et al. 2008) in 2008, April. A concurrent rapid rotation of the PA was also observed just after the maximum in optical flux had been reached (Larionov et al. 2008). This seems to support the indication observed in previous MAGIC observations for other BL Lac objects (Albert et al. 2006, 2007) that there is a connection between the optical high states and VHE γ-ray high states.

The recent optical monitoring of S5 0716+714 shows a consistent rising trend in the R-band flux over the past few months. The older observations reveal that the source had gone to a very faint state (14.9 mag in the R band) around 2013, December (MJD 56650), which is very close to the faintest state of this source reported till the date (K. S. Baliyan 2015, private communication). Very recently, Carrasco et al. (2015c) reported a high state in IR on MJD 57033.3 (2015, January 11) that was around 2.5 magnitude brighter than the previously observed flux on MJD 57021 (2014, December 29). Following these observations, there were several telegrams reporting further brightening of S5 0716+714 in different optical and IR bands (Arkharov et al. 2015; Bachev & Strigachev 2015; Bachev et al. 2015; Chandra et al. 2015; Spiridonova et al. 2015). Soon after these reports of optical/IR flares, Mirzoyan (2015) reported a variable VHE detection above 150 GeV. This VHE detection, quasi-simultaneous with a high flux state in the optical, seems to be similar to that seen in the 2008 event. In the present work, we investigate this event in the framework of time-dependent modeling of the observables, namely, light curves, SEDs, and multi-frequency polarization, to understand the role of the magnetic field in the blazar jet. Our study is mainly focused on the simulation of the part of the outburst where simultaneous data at all energies (optical to γ-rays) are available. This paper is organized as follows. Section 2 provides the details of data resources and the analysis methodology adopted. We present the multi-wavelength light curves and SEDs along with their modeling in Section 3, followed by a discussion of the results obtained in Section 4. Finally, in Section 5, we present a summary of our work.

2. OBSERVATIONS AND DATA ANALYSIS

We used data from LAT on board the *Fermi* spacecraft (Atwood et al. 2009) for γ-ray counterparts to the optical flaring event. The *Swift*/XRT (Burrows et al. 2005) and *Swift*/UVOT (Roming et al. 2005) data are analyzed for X-rays and UV light curves and SEDs. The optical monitoring data from the 1.2 and 0.5 m telescopes at Mt. Abu Infra-Red Observatory (MIRO) are also analyzed. A few other observations, reported in "The Astronomers Telegrams," are also used in the present study. The corresponding values are corrected for galactic extinction and reddening. Publicly available spectropolarimetric observations from Steward Observatory in Arizona are also used. In the following, we summarize the details of the observations and data analysis techniques used for various data sets.

2.1. Fermi-LAT

LAT normally works in all-sky scanning mode, covering the whole sky every three hours. The scanning mode, along with its large field of view, provide almost 30 minutes of monitoring for each source during the course of each scan. The broad energy coverage of LAT ($\Delta E \approx 0.02$–300 GeV) makes this facility ideal for studying high-energy astronomical events.

Two months of *Fermi*-LAT *P7REP* data from 2015 January 01 to March 01 were analyzed using the *Fermi* ScienceTools *v9r33p0*. In the analysis, only SOURCE class events with energies between 100 MeV and 200 GeV, defined under the Instrument Response Function *P7REP_SOURCE_V15*, from a 15° region of interest (ROI) centered at the location of S5 0716 +714 (R.A. = 110°.473, decl. = +71°.343) have been used. We have not included the low-energy and high-energy ends of the LAT data to avoid possible contamination by artificial counts caused by the poor response of the detector in this range. All of the sources from the 2FGL catalog (Nolan et al. 2012) within the ROI, plus an annular radius of 10° around it, were modeled along with the standard diffuse templates of Galactic (*gll_iem_v05_rev1.fit*) and isotropic background (*iso_source_v05_rev1.txt*). To generate the XML model file, we made use of the contributory python package, make2FGLxml.py.[6] The criterion for using a proper model for generating light curves and SEDs is similar to that adopted by Chandra et al. (2014) and Kushwaha et al. (2014). At first, all of the sources within ROI+10° were considered for unbinned likelihood analysis. The point sources with TS values less than 0, obtained from likelihood analysis, were removed from our input model. The likelihood analysis procedure was repeated until it converged without any source with TS < 0. The daily fluxes for the light curves were then extracted using the best model parameters where both spectral indices and normalization were

---

[6] http://fermi.gsfc.nasa.gov/ssc/data/analysis/user/

Table 1
Swift XRT Spectral Fitting Parameters

ObsID	Exposure (s)	Time (MJD)	Sp. Index (Γ)	$\log_{10}(F_{0.3-10.0\,\text{keV}})$ (erg cm^{-2} s^{-1})	χ^2	dof
00035009145	1043	57023.21	2.3 ± 0.4	-11.4 ± 0.10	4.6	3
00035009146	821	57029.01	1.9 ± 0.4	-11.3 ± 0.13	1.6	2
00035009147	976	57041.09	2.7 ± 0.3	-11.0 ± 0.06	5.0	11
00035009148	1091	57042.75	2.4 ± 0.2	-10.9 ± 0.06	14.1	13
00035009149	961	57043.41	1.8 ± 0.6	-10.7 ± 0.20	1.7	3
00035009152	1348	57044.02	2.3 ± 0.2	-10.7 ± 0.05	23.1	19
00035009153	6895	57044.29	2.3 ± 0.1	-10.8 ± 0.03	38.4	50
00035009154	978	57045.01	2.5 ± 0.3	-10.6 ± 0.06	6.6	9
00035009156	9574	57045.14	2.5 ± 0.1	-10.7 ± 0.02	92.2	89
00035009157	1688	57047.14	2.6 ± 0.1	-10.6 ± 0.03	17.2	26
00035009158	6557	57047.22	2.6 ± 0.1	-10.6 ± 0.02	79.8	68

kept free. However, to generate the SEDs, spectral indices in the model were kept fixed at -1.6 ± 0.01 as obtained from the likelihood analysis of the complete data set.

2.2. Swift Data Analysis

The 0.3–10.0 keV X-ray and UV/optical archival data from XRT and UVOT instruments on board the *Swift* X-ray space-borne observatory (Gehrels et al. 2005) were analyzed for the present work. The standard procedures prescribed by the instrument teams were followed step by step to generate the science products. For our analysis, we used the recently updated version of the calibration database (CALDB) along with *heasoft v6.16*. A number of pointings made by *Swift* during 2015 January 19–31 were analyzed. The following is a quick summary of the analysis procedures used for XRT and UVOT data.

2.3. XRT Data

The level 2 cleaned event files were generated using the standard *xrtpipeline* tool with default parameters setting and following the prescriptions of the instrument team. The source and background light curve and spectra were generated with appropriate region and grade filtering using the *xselect* tool. In this case, the source spectrum was extracted for a circular region of 47″ radius around the source location while four source-free regions in the neighborhood of the target, each with a 100″ radius, served for the background spectrum. The count rate in these observations exceeded the recommended pile-up free count rate for PC mode (0.5 counts s^{-1}). Therefore, all of the event files were investigated for pile-up and a proper procedure for pile-up correction, as suggested by other researchers,[7] was used wherever needed. The ancillary response matrix was generated using the task *xrtmkarf* followed by the *xrtcentroid* task. The response matrix file provided with the CALDB distribution was used for further analysis.

Spectral fitting was done in the energy band between 0.3 and 10.0 keV using the XSPEC (version 12.8.2) package distributed with the *heasoft* package. A simple power law along with Galactic absorption gives the best fit for almost all of the observations of interest. The model parameter N_H, i.e., the equivalent Galactic neutral hydrogen column density, was kept fixed at a value of 3.06×10^{20} cm^{-2} (Kalberla et al. 2005, 2010). This value was estimated using the web-based tool

developed by a group at the University of Bonn.[8] The normalization and spectral index of the power law were the free parameters for the spectral fitting. Table 1 summarizes the values of various parameters obtained from the spectral fitting for different observation IDs. The 0.3–10.0 keV fluxes thus obtained were used to construct the light curves.

The Galactic absorption-corrected X-ray energy spectrum was constructed using the procedure adopted in Chandra et al. (2014), except that instead of using the default binning, all of the spectra files were binned according to a fixed input file (describing the details of channel binning) using the *grppha* tool. Multiple X-ray spectra, if any, for a particular SED segment were merged keeping in mind the possible spectral variations.

2.4. UVOT Data

UVOT snapshots with all six available filters, V (5468 Å), B (4392 Å), U (3465 Å), UVW1 (2600 Å), UVM2 (2246 Å), and UVW2 (1928 Å), for all of the ObsIDs were integrated using the *uvotimsum* task and analyzed using the *uvotsource* task, with a source region of 5″, while the background was extracted from an annular region centered on the source location with external and internal radii of 40″ and 7″, respectively. The fluxes thus obtained were corrected for galactic extinction using a tool developed for the R platform. This interactive tool adopts the model described in Cardelli et al. (1989). This tool needs the $E(B-V)$ value as input, which was estimated using the web-based calculator by the NASA/IPAC Infrared Science Archive[9] (Schlafly & Finkbeiner 2011). The value of this parameter in the direction of S5 0716+714 is 0.026 ± 0.001. The extinction-corrected fluxes obtained from the aforementioned procedures were then used to extract the light curves and SEDs.

2.5. Optical Photometry and Polarization Data

Photometric monitoring of S5 0716+714 was performed using the iKon ANDOR CCD Camera (2048×2048) as a backend instrument at the $f/13$ Cassegrain focus of the 1.2 m optical telescope of MIRO. The CCD in this camera is cooled to $-80°$ with thermoelectric (TE) cooling to keep the dark current very low. The camera is attached to a coupling unit consisting of a filter wheel with 12 slots, equipped with 10

---

[7] http://www.swift.ac.uk/analysis/xrt/pileup.php

[8] https://www.astro.uni-bonn.de/hisurvey/profile/index.php
[9] http://irsa.ipac.caltech.edu/applications/DUST/

optical filters (Standard Johnson/Cousins UBVRI broadband filters+u, g, r Sloan filters + two narrow band filters) just on top of the camera. One of the two additional slots remains blocked to grab bias/dark frames, whereas the other is kept open for white light monitoring of extremely faint sources. The bias and sky flats were taken on a daily basis to perform pre-photometric image processing. The source was also monitored using the Automated Telescope for Variability Studies (ATVS) at MIRO mounted with the TE cooled ($\sim -80^\circ$) ANDOR iXon EMCCD camera (1024×1024) as the backend instrument. This camera is coupled with a filter wheel with the Standard Johnson/Cousins UBVRI filters. The twilight sky flats and bias frames were also captured on a daily basis. The observing strategy for both the facilities was to capture a few images in all of the bands (UBVRI) and then monitor for a longer time in one filter, say the R band. The apparent magnitudes of the source and the known field stars (photometric standards) for individual exposures were derived using the standard aperture photometry technique preceded by pre-processing of images (Chandra et al. 2011, 2014). The magnitude was then converted into flux using simple conversion factors and zero point flux for different bands (Bessell 1979). Apart from photometric monitoring at MIRO, the observed fluxes from various Astronomers Telegrams were also used for comparison and completeness. The R-band fluxes obtained from the Steward observatory database are also used followed by extinction correction.

The optical polarimetric data used in this study were taken from the observations performed as part of the *Fermi* Support observing Program at Steward Observatory, Arizona, USA (Smith et al. 2009). The PD and PA values provided in the Steward observatory database are already calibrated, and hence can be readily used. We have corrected the PA values for 180° angle ambiguity in order to make the rotation clearly visible (Figure 1(f)).

3. RESULTS AND INTERPRETATION

The multi-wavelength light curves derived using observational data from various resources, mentioned in Section 2, are shown in Figure 1. The SED for the duration of MJD 57045.5–57047.5 was also generated using data from the aforementioned facilities. In the following, we discuss the results and their interpretations.
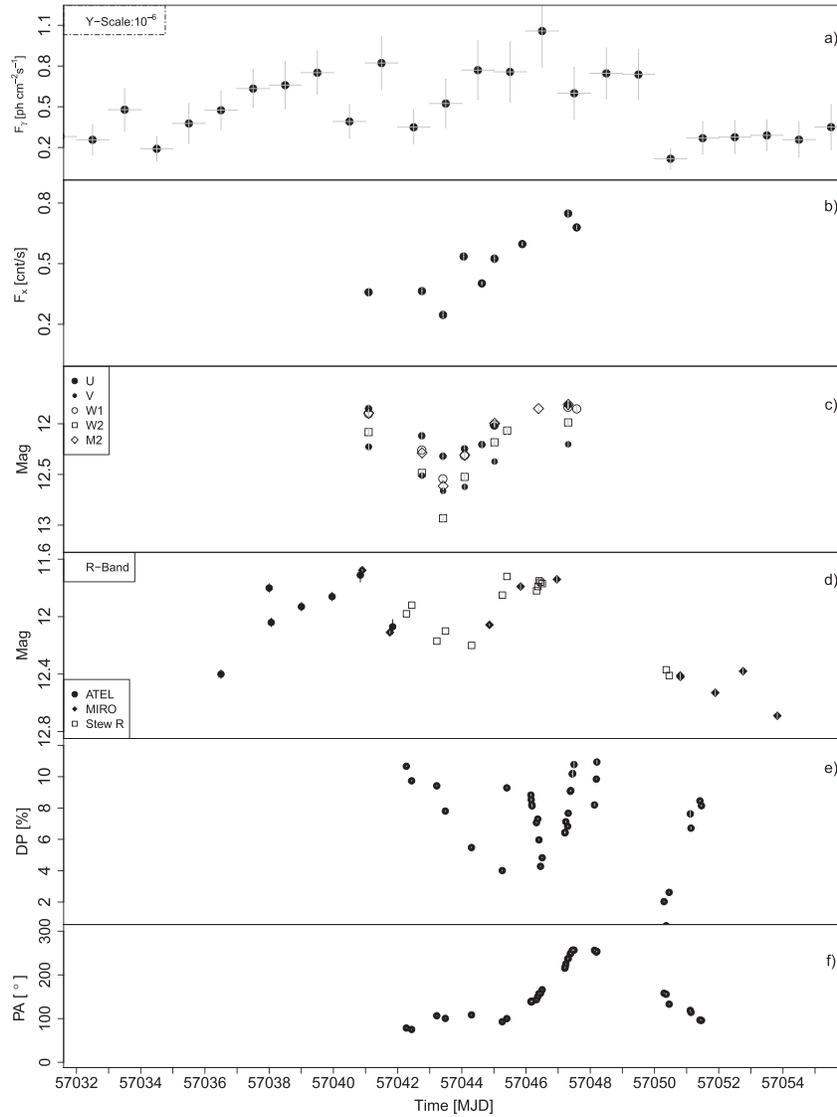
3.1. Multi-wavelength Light Curves

Figures 1(a) and (b) show the γ-ray and X-ray fluxes observed by *Fermi* and *Swift*, respectively. Figure 1(c) shows the UV/optical light curves derived from UVOT observations, while Figure 1(d) shows the R-band magnitudes from various resources. Figures 1(e) and (f) are the PD and PA observations from Steward observatory. The figures show significant variability in all of the energy bands (γ-rays to UV/optical) as well as in optical polarization. As is evident from Figure 1(a), γ-rays show a clear trend of multiple ups and downs during the span of MJD 57034–57055. A consistent rise in flux is seen between MJD 57034.5 and 57039.5, reaching a flux level of 0.75×10^{-6} ph cm^{-2} s^{-1} which is about 4 times the average γ-ray flux of this source. A rapid variation in flux is seen during MJD 57040.5–57042.6 reaching a flux level of 0.83×10^{-6} ph cm^{-2} s^{-1} on MJD 57041.5, i.e., within one day the flux increased and then decreased to 0.35×10^{-6}

ph cm^{-2} s^{-1} the next day. The flux again started rising slowly after MJD 57042.5 and reached to 1.1×10^{-6} ph cm^{-2} s^{-1}, the highest γ-ray flux level reported for this source. However, a fast decrease in flux soon after this flare was also observed. We therefore note two major γ-ray sub-flares associated with the 2015 January major flare in S5 0716+714 . The *Swift* X-ray light curve in the 0.3–10.0 keV band (Figure 1(b)) exhibits a consistently rising trend with a peak flux of $2.7 \pm 0.3 \times 10^{-11}$ erg cm^{-2} s^{-1} on MJD 57047.2, which is comparable to the peak X-ray flux seen during the 2007 October–November flare of S5 0716+714 (Giommi et al. 2008). The poor coverage of the XRT observations restricts us from making conclusions about multiple sub-flares in X-rays. However, the ups and downs in the individual data points provide a glimpse of small-scale variations.

The R-band optical light curve (Figure 1(d)), shows two distinct, well-separated sub-flares. Initially, the R-band flux slowly rises and reaches 11.6 mag from 12.41 mag during MJD 57035–57041.3 (rate $\sim$0.13 mag day^{-1}). The peak flux here corresponds to the brightest ever reported state of the source (Chandra et al. 2011). Just after this peak, the flux decreases to 12.22 magnitude between MJD 57040.5 and 57044.4 (0.14 mag days^{-1}). Here, we have ignored variations in subsequent nights. Specifically, the source underwent a very fast decrease in flux ($\Delta M \sim 0.5$ mag) during MJD 57040–57041.8 and then again went to 11.9 mag on MJD 57042.4 before falling to 12.2 mag on MJD 57044.2. Soon after, the R-band flux again started rising at a slightly faster rate (0.33 mag day^{-1}). The peak flux corresponding to the second bump is almost equal to that of the first one. However, the flux value of the second bump remained constant for quite some time ($\sim$2 days). After this, the flux gradually decreased to 12.68 mag within MJD 57046–MJD 57054.5 (rate $\sim$0.1 mag day^{-1}). Later monitoring suggests an even fainter state of this source. Note that the plotted flux values represent fluxes averaged over a few hours of monitoring. The fluxes in the other optical bands, namely, V, B and I, also show similar behavior but are omitted from the light curves for the sake of clarity in Figure 1. Figure 2 depicts the correlation between fluxes in different optical bands and the flux-dependence of the $B - V$ color. The fluxes in various optical bands are differently correlated, which is clearly seen from the slopes of the best linear fits to these curves (Figure 2). The second panel of Figure 2 represents the standard "bluer when brighter (BWB)" trend seen during a typical flare in blazars. The Swift-UVOT observations (Figure 1(c)) also indicate the existence of two humps in the light curve. However, poor coverage by *Swift* pointing provides an incomplete picture of the flux variations.

The variations in the optical PD and PA are presented in the Figures 1(e) and (f), respectively. The PD shows various episodes of rapid variation with trends completely unrelated to the total flux variations. More specifically, at the very beginning of our available data set, i.e., around MJD 57042, when S5 0716+714 had already passed through the first optical sub-flare, the PD was very high ($10.67\% \pm 0.02\%$), and then decreased to $4.0\% \pm 0.02\%$ by MJD 57045.3. The next two observations reveal a 5.4% change in PD between two epochs in the same night differing by 2.4 hr (MJD 57045.3–57045.4). The next episode of PD is even more dramatic and nicely covered as the PD decreases by 4.68% within $\sim$ 7.2 hr (8.88%–4.20% between MJD 57046.2 and MJD 57046.5). In the next three segments, namely, MJD 57047.2–57047.5, MJD

Figure 1. Multi-wavelength light curve of S5 0716+714 showing the recent outburst activity during 2015, January. Figures 1(a) and (b), respectively, represent *Fermi* (>0.1 GeV) and X-ray (0.3 10.0 keV) light curves, whereas Figures 1(c) and (d) present UV/optical magnitudes from *Swift*-UVOT and MIRO, respectively. The last two panels (1(e) and (f)) are PD (or DP) and PA variations. The "Stew R" notation in Figure 1(d) stands for the R-band data from Steward Observatory.

57048.1–57048.2, and MJD 57050.3–57051.5, independent rising trends of 4.4% (6.38%–10.79%), 2.96% (8.0%–10.96%), and 8.01% (0.45%–8.46%), respectively, are seen. The typical error in these observations of PD is 0.02%. A straight line was fit to the individual segments of PD variations using a least-square fitting algorithm, which clearly indicates very different slopes for all of them (L1–L5 in left panel, Figure 3). It is very difficult to associate rapid fluctuations in PD with the double-humped shaped variation in the total flux light curve. It could perhaps be due to two emission components contributing to the total flux, one nearly unpolarized and the other polarized, both varying with time. The observed PA profile also supports the same argument, as discussed below. Initially, during the first segment of the PD variations (MJD 57042.3–57045.3), the PA is mildly variable around 100° with a slight change from 78°.6 to 100°.2. This implies the decay of a previously polarized component and the emergence of a new one, both with similar PA. Afterwards, the new polarized component starts to evolve. During MJD 57045–57047.5, the PA consistently increases by ∼164°, from 93°.0 to 256°.9. Later observations (MJD

57048.1–57051.5) suggest a consistent decrease in PA from 256°.9 to 96°. The rising and falling parts of the PA variations were fit with an exponential function [$f(x) \sim A e^{-\alpha(x-x0)}$] to get an estimate of the temporal profile (right panel, Figure 3). The index of the exponential for the rising part is -0.45 ± 0.01 day^{-1}, whereas that for the falling part is 0.29 ± 0.006 day^{-1}. This shows that the second PA swing is slower than the first (right panel, Figure 3). These make the case for two rotations of about 180° each during the course of the second optical sub-flare, indicating the sub-flare to be strongly related to a significant change in the magnetic field.

Mirzoyan (2015) reported MAGIC detection of the variable VHE γ-ray flux in the range 4×10^{-11}–7×10^{-11} ph cm^{-2} s^{-1} above 150 GeV during MJD 57044–57048, which is simultaneous with the X-ray and optical high states of S5 0716+714 during the second sub-flare (Figure 1). It appears that this variable VHE detection is correlated with the activity in the optical and the X-rays, similar to the 2008 detection of the VHE γ-ray emission of S5 0716+714 (Anderhub et al. 2009).
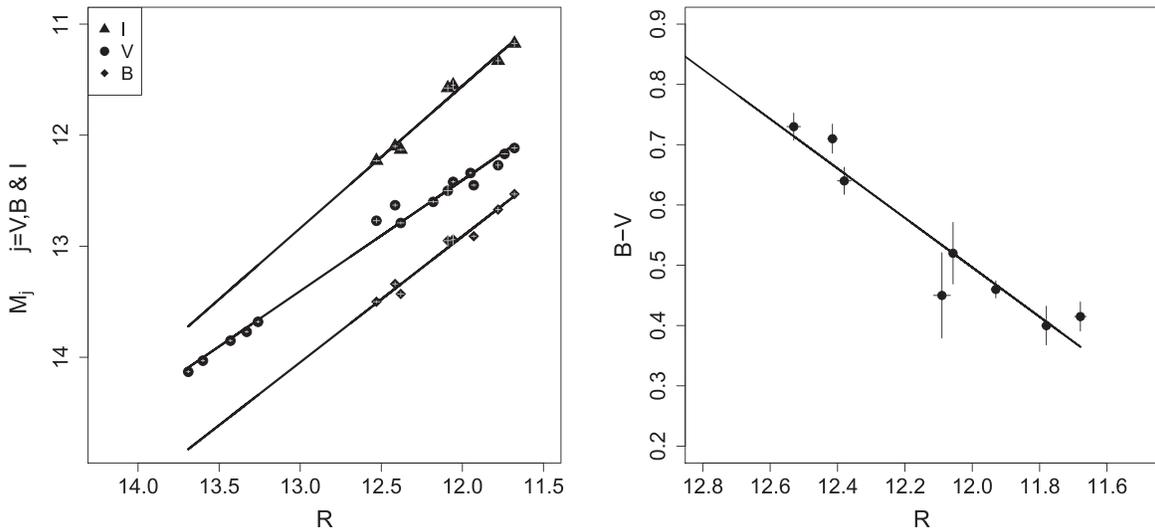
Figure 2. Left: R band and I, V, and B optical band correlation curves for fluxes in different optical bands. The X axis shows the R-band magnitude, whereas the Y axis represents magnitudes in other optical bands, namely, I, B, and V. Right: the flux-color plot for optical observations. The X and Y axes are the R-band magnitude and (B − V) color, respectively.

In the following, we describe the modeling of the observables derived for the duration of MJD 57045.5–57047.5.

3.2. Modeling of Light Curves, Optical Polarization, and SED

In general, there are two mechanisms, namely, shocks and magnetic reconnection, that may result in flaring activity in a blazar jet. We have used the HMFM model proposed by Zhang et al. (2014) to fit the first PA rotation from MJD 57045.5 to 57047.5 (the rising part). This model assumes an axis-symmetric cylindrical geometry for the emission region, which is further evenly subdivided into zones in radial and longitudinal directions (see Figure 1, Zhang et al. 2014). The relativistic plasma in the emission region, pervaded by a helical magnetic field with a possible additional turbulent component, moves on a straight trajectory along the jet and encounters a flat stationary disturbance. The disturbance will temporarily modify the physical conditions (magnetic field, particle distribution, etc.) at its location inside the emission region. The initial state in the emission region is regained once it moves out of the shocked region. The non-thermal particle evolution, radiation, and polarization signatures of our model are realized by the Monte-Carlo/Fokker–Planck radiation transfer code developed by Chen et al. (2012) and the 3D polarization dependent radiation transfer code developed by Zhang et al. (2014). In this model, the particle distributions in individual zones are evolved using a locally isotropic Fokker–Planck equation, and the polarization-dependent emission from each zone is properly traced to account for all the LTTEs. Even if the disturbance in our model is flat, the flaring region, which consists of the zones affected by the disturbance whose emissions arrive to the observer at the same time, will be distorted into an elliptical shape. Illustrations of the model setup and the LTTEs can be found in Figure 4 and Zhang et al. (2015).

Table 2 lists some key parameters from our modeling, estimated in the comoving frame of the emission region. Due to the relativistic aberration, even though we are observing these objects at very close alignment to the relativistic jet in the observer's frame (typically, $\theta^*_{obs} \sim 1/\Gamma$, where Γ is the bulk

Lorentz factor of the outflow along the jet), the angle θ_{obs} between LOS and the jet axis in the comoving frame is likely to be much larger. Specifically, if $\theta^*_{obs} = 1/\Gamma$, then $\theta_{obs} = 90°$. In our fitting, we choose the LOS in the comoving frame at $\theta_{obs} = 90°$. As is mentioned above, the PD variations are hardly linked to the flux variations; thus, an unpolarized turbulent contribution to the total flux is likely to be present. Therefore, we have fitted the averaged SED for the period, which contains a helical component and a constant turbulent contribution, and then fit the polarization signatures based on the derived parameters. Also, the PA profile is fit prior to the PD profile, as the former is less affected by the turbulence. The best-fit model and data are displayed in Figure 5.

We assumed a leptonic origin for the SED, so that the low-energy component is dominated by synchrotron while the high-energy component consists of both SSC and EC contributions. Due to the Monte-Carlo photon tracing, small numerical errors are present but the overall fitting is very close to the data. The time-dependent polarization profiles are interpreted as alterations in the magnetic topology initiated by the disturbance. The origin of the disturbance can be either shock or shock-initiated magnetic reconnection. Before the emission region encounters the disturbance, the entire region contributes uniformly. Although the helical magnetic field has comparable poloidal and toroidal contributions, due to the axis-symmetry of the emission region and the LOS orientation, the projected poloidal contribution onto the plane of sky is stronger, resulting in a poloidal-dominating polarized flux. When the disturbance moves in, it will alter the local magnetic field to be toroidal-dominating. In addition, it will strengthen the emission in this region by amplifying the local magnetic field strength (shock) or injecting additional non-thermal electrons (reconnection). Due to the LTTEs, only the near side of the flaring region is observed at first, so that the PD gradually drops as the initial poloidal dominance is balanced by the flaring toroidal contribution, and the PA rotates toward toroidal component. At the middle of the event, the flaring region will extend across the emission region, and therefore it will receive equal contributions from both the near and the far sides (Figure 4), as seen from the observer, mimicking the initial axis-symmetry
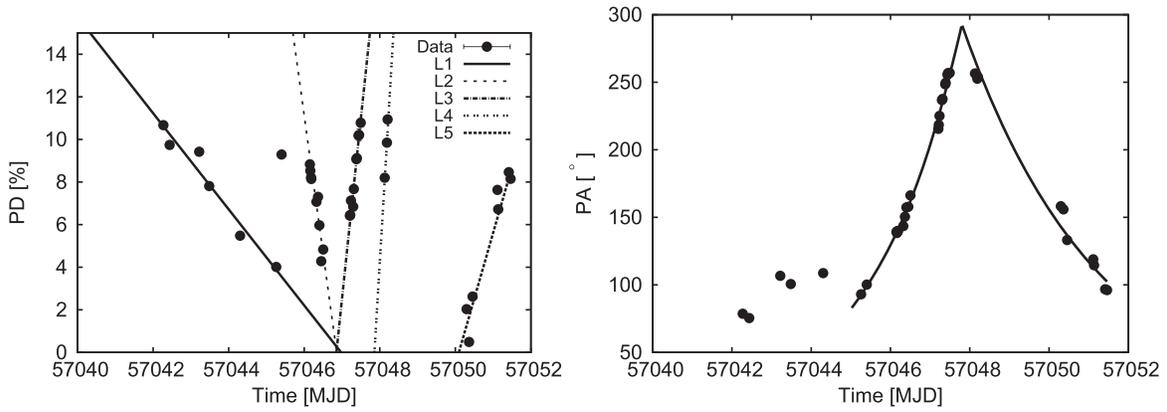
Figure 3. Left: the PD variation with individual segments fit by straight lines (L1–L5). The fitting is performed using a least-square fitting algorithm. Right: the PA variations fit with an exponential rising and falling profile given by $[f(x) \sim A e^{-\alpha(x-x0)}]$.

but dominated by toroidal contribution. Since the length of the cylindrical emission region is longer than its diameter, this flaring region will stay for some time, creating a "step phase" in both PD and PA profiles, as proposed in Zhang et al. (2015). After that, the disturbance will completely leave the emission region and the flaring region moves to the far side so that the PD reverts back to its initial state in a time-symmetric pattern. The PA instead completes a 180° rotation to the initial state (notice the 180° ambiguity) because the projected toroidal component on the near side is opposite to that on the far side.

We have further investigated a few issues in the polarization fitting. We note that although the decreasing part of the PD profile is well reproduced, the rising part around MJD 54047 is a bit off. We remind readers that we have applied a constant unpolarized turbulence in our fit, which in reality may decrease with time, and consequently PD may increase. The PA, however, is generally unaffected. Moreover, the "step phase" is indeed necessary and can place a strong constraint on the ratio of the length and diameter of the emission region. We can see in the data that both PD and PA tend to converge at a stable value during the middle of the event. Most importantly, the slopes of the PA rotation before and after the "step phase" set a stringent constraint on the ratio of the flaring toroidal dominance to the initial poloidal dominance. This ratio not only leads to a definite excess of toroidal contribution during the "step phase," which is shown in the PD profile, but also requires the helical component to undergo an increment in the flux. This is consistent with the flare activity observed at X-rays and γ-rays. During the PA rotation, the total optical flux is almost stabilized at its highest observed flux and hardly shows any pattern. Therefore, to compromise the flare in the helical component, the turbulent contribution has to decrease, further confirming our previous assumption.

4. DISCUSSION

The observations of simultaneous variations in multi-wavelength bands shown in Figures 1(a)–(f) suggest that similar activity is driving the emission over a broad range of the spectrum during the brightness phase of S5 0716+714 . The fact that the flare is seen almost simultaneously over a broad spectrum further suggests that the emission region is likely to be co-spatial. Additionally, it indicates that the region of maximum dissipation should be transparent to emission at all energies. The variable VHE detection that followed the activity

in the optical along with the historically bright state in X-rays and γ-rays, coinciding with variable PD and rotation of PA, imply that the same electron population is responsible for this major activity. In short, in our model, these observations support a leptonic origin for the high-energy emission during the 2015 activity of S5 0716+714 . A careful look at Figures 1(a)–(f) reveals the occurrence of two major sub-flares in all of the bands, super-imposed with small amplitude fluctuation. Any analysis of the time lag between the different wavebands, however, is difficult to perform due to the limited coverage and their resolution in the present data. The BWB trend and the different slopes in the flux–flux correlation graph (Figure 2) indicate that this flare may have been caused by shock acceleration activity in the jet rather than being triggered by the involvement of geometry dependent effects. The very rapid (hourly) and prominent variations in PD reflect the crucial role played by the magnetic field during this event. The individual segments of PD variations may be due to fluctuations in the shocked region resulting in changes in the magnetic field in the compressed region.

The variations in PA observed during the second optical sub-flare are the most important feature of this state. There is a clear indication of rotation in PA, almost coincident (within a day) with the optical, X-ray, and γ-ray flares. This particular scenario is well observed in some blazars, namely, 3C279, Mrk421, PKS 1510–089, etc. (Abdo et al. 2010; Marscher et al. 2010; Marscher 2014). Several mechanisms have been proposed to interpret the PA rotations, such as an emission region moving along a curved trajectory (Villata & Raiteri 1999), a bending in the jet (Marscher et al. 1991), streamlines following the helical magnetic field lines (Marscher et al. 2008), or stochastic activation of individual zones in a turbulent shock (TEMZ, model). The bending jet model involves an asymmetric jet structure, and thus requires a lot of freedom in the parameter space. Streamlines along a helical magnetic field imply that PA rotation should preferably be in the same direction, while the two sequential PA rotations are observed in opposite directions. Additionally, both models cannot naturally explain the simultaneous flaring activities. The TEMZ model, on the other hand, can hardly produce the systematic, apparently time-symmetric polarization profiles due to its stochastic nature. Nevertheless, our HMFM model applies a simple axisymmetric geometry for the emission region and the disturbance, taking into account all of the LTTEs, naturally explaining the simultaneous flaring activities and the
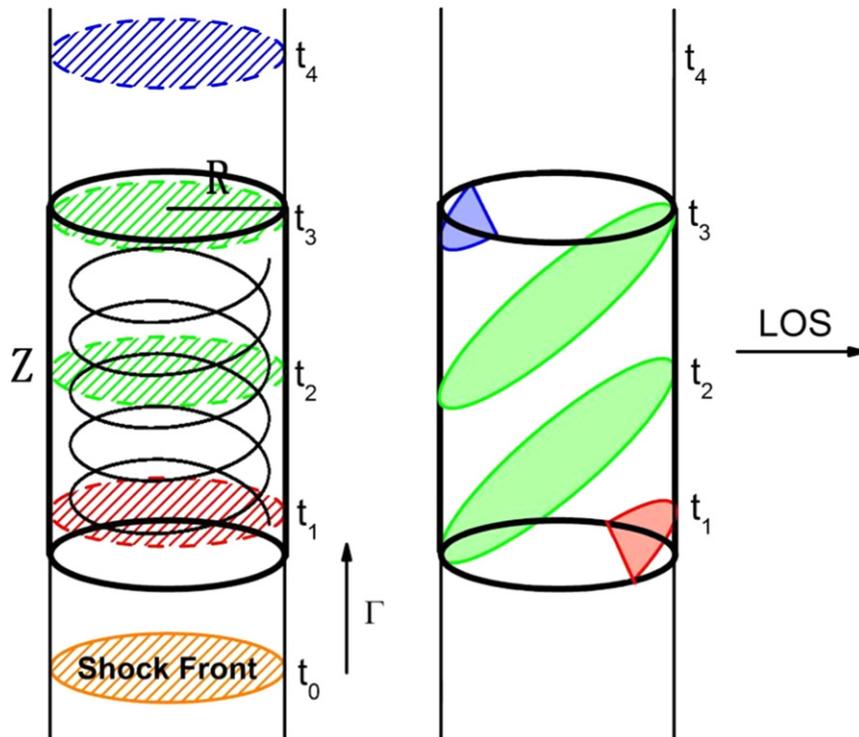
Figure 4. Left: sketch of the interaction between the emission region and the disturbance in the comoving frame of the emission region at different epochs. The emission region is pervaded by a helical magnetic field and a turbulent component (only the helical component is sketched). The disturbance is stationary in the observer's frame, but in the comoving frame of the emission region, the disturbance is then moving up with Lorentz factor Γ. The orange, red, green, and blue regions refer to the locations of the disturbance before the flare (t_0), the rising phase (t_1), peak (t_2 and t_3), and declining phase (t_4), respectively. Right: the red, green, and blue shapes indicate the shape and location of the flaring region, corresponding to the disturbance at $t_1 \sim t_3$, respectively, observed simultaneously, taking into account the LTTEs. Since $Z > 2R$, the peak state will stay for few hours or few days depending upon the Z/R ratio.

Table 2
The Best Estimates of the Model Parameters

| Parameters	Value (CGS)
Bulk Lorentz factor	20
Length of the emission region Z (cm)	6.06×10^{16}
Radius of the emission region R (cm)	2.25×10^{16}
Length of the disturbance L (cm)	6.06×10^{15}
Radius of the disturbance A (cm)	2.25×10^{16}
Orientation of LOS (deg)	90
Electron acceleration time-scale (Z/c)	5.50×10^{-3}
Electron escape time-scale (Z/c)	6.00×10^{-4}
Electron density (cm^{-3})	21.7
Helical magnetic field strength (G)	0.5
Helical pitch angle (deg)	47
Helical pitch angle during flare (deg)	75.5

apparently time-symmetric polarization profiles. In addition, based on the behavior of the disturbance, a PA rotation event immediately following in the opposite direction is possible. However, since the second PA rotation does not have sufficient data coverage, we are unable to constrain the model parameters. This part is omitted in Figure 5.

Our best-fit parameters do not allow us to distinguish between the shock scenario and the shock-initiated reconnection scenario. However, we still prefer the reconnection mechanism because our model predicts higher flare amplitude at high energies than in the optical, as is seen here. In the reconnection, the increase of the non-thermal electron density is due to the dissipation of magnetic energy, which weakens the synchrotron flare. The shock scenario,

however, enhances both the non-thermal density and the magnetic field strength, leading to a stronger synchrotron flare. The aforementioned flare and PA rotation event is very similar to the other flare and PA rotation events seen in blazars (Abdo et al. 2010; Marscher et al. 2010; Marscher 2014; Zhang et al. 2015). After these events, the flux in all bands suffers a large decrease and becomes less active. This indicates that a severe energy dissipation occurs during the flare and PA rotation. PA rotation implies a strong alteration in the magnetic field, which again provides another piece of evidence for reconnection.

5. SUMMARY

S5 0716+714 exhibited a multi-wavelength outburst in January 2015 with two well-resolved sub-flares in gamma-rays and the optical. The event was accompanied by rapid PD variations and a systematic PA swing, and followed by a variable VHE detection ($F_{>150 \, \text{GeV}} = 4$–$7 \times 10^{-11} \, \text{ph cm}^{-2} \, \text{s}^{-1}$) by the MAGIC group. The total flux and PD variations seem to be uncorrelated, due to the significant contributions from the unpolarized component to the total emission. However, our study shows the co-spatiality of emission at high and low energies. The observability of quasi-simultaneous emission provides hints about the location of the emission region in the jet. The color variations and BWB trend indicate that it may likely be of shock and/or shock-initiated reconnection origin. The HMFM model, adopted to simulate the part of outburst, suggests that the magnetic reconnections more likely played a very important role in this event. The rising part of PA rotation is very well fit by a "step phase" profile. The same profile also presents a reasonably good fit for PD variations, except for a slight deviation toward the end. This may be explained by
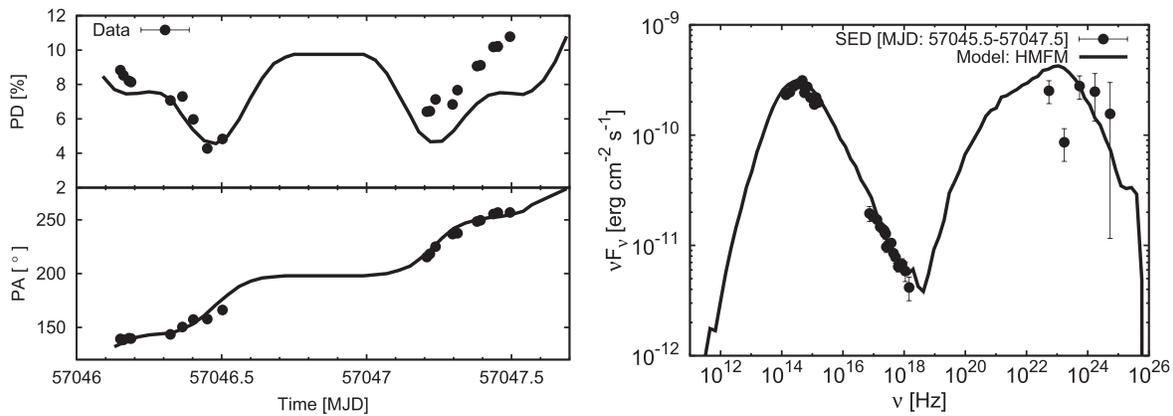
Figure 5. Left: the model reproduced PD and PA, generated for the duration of MJD 57045.5–57047.5. The PD variations overplotted with the modeled curve (thick black line). The bottom panel represents the data and model for the PA swing. Right: the broadband SED of S5 0716+714 for the aforementioned duration. The multi-wavelength light curves and respective models are not shown here as the flux remains almost constant (though highest) for the duration under consideration.

including the contributions of other unpolarized emission components in the optical band. The excess in the ratio of the toroidal component to the poloidal component of the magnetic fields during quiescent and flaring episodes indicates that the helical component contributes to the flux increment (Table 2). In conclusion, our study suggests that this outburst event is more likely to be similar to the 2008 outburst state of S5 0716+714, and was probably triggered by shock-initiated magnetic reconnection taking place in the emission region in the jet.

REFERENCES

Abdo, A. A., Ackermann, M., Ajello, M., et al. 2009, ApJ, 700, 597
Abdo, A. A., Ackermann, M., Ajello, M., et al. 2010, Natur, 463, 919
Agudo, I., Marscher, A. P., Jorstad, S. G., et al. 2011, ApJL, 735, L10
Albert, J., Aliu, E., Anderhub, H., et al. 2006, ApJL, 648, L105
Albert, J., Aliu, E., Anderhub, H., et al. 2007, ApJL, 666, L17
Anderhub, H., Antonelli, L. A., Antoranz, P., et al. 2009, ApJL, 704, L129
Arkharov, A. A., Borman, G. A., Di Paola, A., Larionov, V. M., & Morozova, D. A. 2015, ATel, 6942, 1
Atwood, W. B., Abdo, A. A., Ackermann, M., et al. 2009, ApJ, 697, 1071
Bachev, R., Spassov, B., & Boeva, S. 2015, ATel, 6944, 1
Bachev, R., & Strigachev, A. 2015, ATel, 6957, 1
Bessell, M. S. 1979, PASP, 91, 589
Błażejowski, M., Sikora, M., Moderski, R., & Madejski, G. M. 2000, ApJ, 545, 107
Bloom, S. D., & Marscher, A. P. 1996, ApJ, 461, 657
Burrows, D. N., Hill, J. E., Nousek, J. A., et al. 2005, SSRv, 120, 165
Cardelli, J. A., Clayton, G. C., & Mathis, J. S. 1989, ApJ, 345, 245
Carrasco, L., Porras, A., Recillas, E., et al. 2015c, ATel, 6902, 1
Chandra, S., Baliyan, K. S., Ganesh, S., & Foschini, L. 2014, ApJ, 791, 85
Chandra, S., Baliyan, K. S., Ganesh, S., & Joshi, U. C. 2011, ApJ, 731, 118
Chandra, S., Kushwah, P., Ganesh, S., Kaur, N., & Baliyan, K. 2015, ATel, 6962, 1
Chen, A. W., D'Ammando, F., Villata, M., et al. 2008, A&A, 489, L37
Chen, X., Fossati, G., Böttcher, M., & Liang, E. 2012, MNRAS, 424, 789
Dermer, C. D., Schlickeiser, R., & Mastichiadis, A. 1992, A&A, 256, L27
Ferrero, E., Wagner, S. J., Emmanoulopoulos, D., & Ostorero, L. 2006, A&A, 457, 133
Foschini, L., Tagliaferri, G., Pian, E., et al. 2006, A&A, 455, 871
Gehrels, N., Chincarini, G., Giommi, P., et al. 2005, ApJ, 621, 558
Giommi, P., Massaro, E., Chiappetti, L., et al. 1999, A&A, 351, 59
Giommi, P., Perri, M., Verrecchia, F., et al. 2008, ATel, 1495, 1
Ghisellini, G., Maraschi, L., & Treves, A. 1985, A&A, 146, 204
Ghisellini, G., Tavecchio, F., & Ghirlanda, G. 2009, MNRAS, 399, 2041
Hartman, R. C., Bertsch, D. L., Bloom, S. D., et al. 1999, ApJS, 123, 79
Kalberla, P. M. W., Burton, W. B., Hartmann, D., et al. 2005, A&A, 440, 775
Kalberla, P. M. W., McClure-Griffiths, N. M., Pisano, D. J., et al. 2010, A&A, 521, A17
Kushwaha, P., Singh, K. P., & Sahayanathan, S. 2014, ApJ, 796, 61
Larionov, V., Konstantinova, T., Kopatskaya, E., et al. 2008, ATel, 1502, 1
Marscher, A. P. 2014, ApJ, 780, 87
Marscher, A. P., Jorstad, S. G., D'Arcangelo, F. D., et al. 2008, Natur, 452, 966
Marscher, A. P., Jorstad, S. G., Larionov, V. M., et al. 2010, ApJL, 710, L126
Marscher, A. P., Zhang, Y. F., Shaffer, D. B., Aller, H. D., & Aller, M. F. 1991, ApJ, 371, 491
Mirzoyan, R. 2015, ATel, 6999, 1
Nalewajko, K., Sikora, M., & Begelman, M. C. 2014, ApJL, 796, L5
Nandikotkur, G., Jahoda, K. M., Hartman, R. C., et al. 2007, ApJ, 657, 706
Nilsson, K., Pursimo, T., Sillanpää, A., Takalo, L. O., & Lindfors, E. 2008, A&A, 487, L29
Nolan, P. L., Abdo, A. A., Ackermann, M., et al. 2012, ApJS, 199, 31
Orienti, M., Koyama, S., D'Ammando, F., et al. 2013, MNRAS, 428, 2418
Roming, P. W. A., Kennedy, T. E., Mason, K. O., et al. 2005, SSRv, 120, 95
Schlafly, E. F., & Finkbeiner, D. P. 2011, ApJ, 737, 103
Sikora, M., Begelman, M. C., & Rees, M. J. 1994, ApJ, 421, 153
Sikora, M., Stawarz, Ł., Moderski, R., Nalewajko, K., & Madejski, G. M. 2009, ApJ, 704, 38
Spiridonova, O. I., Vlasyuk, V. V., Moskvitin, A. S., & Bychkova, V. S. 2015, ATel, 6953, 1
Sokolov, A., Marscher, A. P., & McHardy, I. M. 2004, ApJ, 613, 725
Smith, P. S., Montiel, E., Rightley, S., et al. 2009, arXiv:0912.3621
Urry, C. M., & Mushotzky, R. F. 1982, ApJ, 253, 38
Urry, C. M., & Padovani, P. 1995, PASP, 107, 803
Urry, M., & Padovani, P. 2000, PASP, 112, 1516
Villata, M., & Raiteri, C. M. 1999, BL Lac Phenomenon, 159, 489
Wagner, S. J., Witzel, A., Heidt, J., et al. 1996, AJ, 111, 2187
Zhang, H., Chen, X., & Böttcher, M. 2014, ApJ, 789, 66
Zhang, H., Chen, X., Böttcher, M., Guo, F., & Li, H. 2015, ApJ, 804, 58